1 Modelling of street-scale pollutant dispersion by coupled simulation of
2 chemical reaction, aerosol dynamics, and CFD

3   Chao Lin [a,*,★], Yunyi Wang [b,★], Ryozo Ooka [c], Cédric Flageul [d], Youngseob Kim [b],
4   Hideki Kikumoto [c], Zhizhao Wang [b], Karine Sartelet [b]
5 [a] Graduate School of Engineering, The University of Tokyo, 4-6-1 Komaba, Meguro-ku,
6 Tokyo 153-8505, Japan
7 [b] CEREA, École des Ponts ParisTech, EdF R&D, 77 455 Marne la Vallée, France
8 [c] Institute of Industrial Science, The University of Tokyo, 4-6-1 Komaba, Meguro-ku,
9 Tokyo 153-8505, Japan
10 [d] Curiosity Group, Pprime Institute, Université de Poitiers, CNRS, ISAE-ENSMA,
11 Chasseneuil, France
12 [*] Corresponding author, c-lin415@iis.u-tokyo.ac.jp
13 ★These authors contributed equally to this work.

14

15 ABSTRACT
16 In the urban environment, gas and particles impose adverse impacts on pedestrians' health.
17 The conventional computational fluid dynamics (CFD) methods that regard pollutant as
18 passive scalar cannot reproduce the formation of secondary pollutants and lead to
19 uncertain prediction. In this study, SSH-Aerosol, a modular box model that simulates the
20 evolution of gas, primary and secondary aerosols, is coupled with the CFD softwares
21 OpenFOAM and Code_Saturne. The transient dispersion of pollutants emitted from
22 traffic in a street canyon is simulated using unsteady Reynolds-averaged Navier–Stokes
23 equations (RANS) model. The simulated concentrations of NO_2, PM_{10} and black carbon
24 are compared with field measurements on a street of Greater Paris. The simulated NO_2
25 and PM_{10} concentrations based on the coupled model achieved better agreement with
26 measurement data than the conventional CFD simulation. Meanwhile, the black carbon
27 concentration is underestimated, probably partly because of the underestimation of non-
28 exhaust emissions (tyre and road wear). Aerosol dynamics lead to large increase of
29 ammonium nitrate and anthropogenic organic compounds from precursor-gas emitted in
30 the street canyon.

31

34

1. Introduction

36 Traffic-related pollutants can impose adverse effects on pedestrians' health in the urban

37 environment (Anenberg et al., 2017; Jones et al., 2008). Especially, particulate matter

38 (PM) is strongly associated with increased cardiovascular diseases (Du et al., 2016).

39 Therefore, investigating the dispersion of PM and the corresponding precursor gas is of

40 great significance to evaluate the environmental impact and devise suitable

41 countermeasures (Kumar et al., 2008).

42 With the development of numerical simulations, computational fluid dynamics (CFD) has

43 been widely used for near-field dispersion prediction (Tominaga and Stathopoulos, 2013).

44 The pollutant dispersion patterns in complex geometric and non-uniform building

45 configurations can be well predicted using CFD simulations (Blocken et al., 2013).

46 Pollutant dispersion, deposition and transformation (chemical reactions and aerosol

47 dynamics) have primary roles in near-field prediction models. However, most CFD-based

48 studies assume that the time scale of transport at the street scale (~ 100 m) is relatively

49 shorter than the time scale of deposition and transformation; therefore, they frequently

50 regard pollutants as inert matter. Meanwhile, the recirculation flows which commonly

51 exist in street canyons lead to low-ventilation zones and may provide sufficient time for

52 transformation (Lo and Ngan, 2017; Zhang et al., 2020).

53 In addition, when PM is transported as a passive scalar, the distribution of the total

54 concentration can be simulated, however, information on the particle size distribution and

55 chemical composition is unclear. Understanding the size distribution is important for

56 evaluating the health hazards because large particles are deposited in the mouth and upper

57 airways, whereas smaller particles deposit deeper in the lungs and can even reach the

58 alveolar region of the lungs (Sung et al., 2007). In addition, as particles of different

59 chemical compositions are related to different sources and/or precursor gases, gaining

60 knowledge of their composition may help devise countermeasures to limit their

61 concentrations (Kim, 2019).

62 To simulate pollutant concentrations considering both transport and transformation, many

63 studies have coupled air-quality models with gas-phase chemistry and aerosol modules

64 and achieved chemical transport from a regional scale (~100 km) (Sartelet et al., 2007) to

65 a street scale (Lugon et al., 2021b). However, few models can simultaneously represent

66 detailed particle dispersion in a complicated urban flow field considering secondary

67 aerosol formation.

68 For the recent development and application of CFD-chemistry coupling model, Kurppa

69 et al., (2019) implemented a sectional aerosol module into large eddy simulation (LES),

70 and conducted a particle dispersion simulation on a neighborhood scale. Gao et al., (2022)

71 employed the same model to examine the dispersion of cooking-generated aerosols in an

72 urban street canyon. In both studies, the effect of particle dynamics on aerosol number

73   concentration was well reproduced. However, the simulated chemical composition was
74   not detailed. In addition, the chemical reactions of the precursor gas were not considered.
75   Kim et al., (2019) coupled unsteady Reynolds-averaged Navier-Stokes (RANS) model
76   with gas chemistry and aerosol modules and conducted simulations of PM_1 in a street
77   canyon under summer and winter conditions. The diurnal variations, spatial distribution
78   and chemical composition of pollutants in the street canyon were investigated. However,
79   the size distribution of particles and the secondary organic aerosol (SOA) chemistry were
80   not considered. Therefore, a more comprehensive coupled model is needed to simulate
81   the evolution of gas concentrations, mass and number concentrations of primary and
82   secondary particles at the same time.

83   Vehicles are considered to be the main ammonia (NH_3) source in urban environments
84   (Sun et al., 2017). Reactive nitrogen emissions from many new vehicles are now
85   dominated by NH_3 (Bishop and Stedman, 2015). Since the formation of ammonium
86   nitrate is often limited by HNO_3 rather than NH_3 in urban areas (NH_3-limited), increasing
87   NH_3 may lead to increased ammonium nitrate production and PM concentration in urban
88   streets (Lugon et al., 2021b). However, NH_3 emissions from passenger cars are usually
89   not regulated (Suarez-Bertoa and Astorga, 2018). Therefore, to provide evidence in
90   making policies for NH_3 emission regulation, it is important to investigate the local
91   influence of NH_3 emissions on PM concentrations.

92   Therefore, to achieve a more comprehensive simulation of PM and related precursor gas,
93   this study couple two open-source CFD softwares: OpenFOAM (OpenFOAM user guide)
94   and Code_Saturne (Archambeau et al., 2004), with gas-phase chemistry and aerosol
95   module SSH-Aerosol (Sartelet et al., 2020). Both OpenFOAM and Code_Saturne own
96   wide users. Therefore, coupling SSH-aerosol with both CFD softwares may satisfy more
97   needs. Simulations of the PM concentrations in a two-dimensional street canyon are
98   conducted. The coupled model is validated by comparison to field measurements. The
99   size distributions and chemical compositions of particles from the models with and
100   without secondary aerosol formation are compared. In addition, cases with large NH_3
101   emissions are considered and the related PM increase is investigated.

102   The remainder of this paper is organized as follows. The coupling of the aerosol model
103   and CFD is introduced in Section 2. The computational details are presented in Section 3.
104   In Section 4, the simulated pollutant concentrations are compared with field
105   measurements, followed by evaluations of the influence of the grid, coupling method and
106   time step. In Section 5, spatial and temporal variations in the concentrations are analyzed.
107   The chemical compositions and size distributions of the particles between the coupled
108   model and the model that does not consider gas chemistry or aerosol dynamics are

109   compared. In addition, the effect of NH_3 traffic emissions on particle concentrations is

110   discussed. Finally, the conclusions and perspectives are presented in Section 6.

111

112   **2. Model description**

113   The coupling method between CFD and chemistry modules is similar to the literature

114   (Gao et al., 2022; Kurppa et al., 2019). OpenFOAM v2012 and Code_Saturne 6.2 are

115   used to solve the governing equations of the flow field and transport equations of gas and

116   particle mass fractions. The inflow conditions, pollutants' background concentrations and

117   emission rates are obtained from regional models, and are linearly interpolated into each

118   time step, which will be introduced in Section 3. This simulation method is called

119   transient-condition method (TCM) in this study. However, because time-varying flow

120   fields and concentration fields are expensive to compute in terms of computational time,

121   conducting CFD simulations with fixed boundary conditions and emission rates at

122   specific time points is considered a practical method for evaluating street-level pollutant

123   concentrations (Wu et al., 2021; Zhang et al., 2020). The transport (advection and

124   diffusion) and chemical processes will reach equilibrium, and the simulated

125   concentrations will reach quasi-stable values. These values are often regarded as time-

126   averaged concentrations. This method is called the constant-condition method (CCM) in

127   this study, in contrast to TCM. However, the simulation accuracy of CCM has not been

128   validated in simulations that consider both gas chemistry and particle dynamics.

129   Therefore, validation is conducted using boundary conditions and emission rates at

130   specific time points and the simulated concentrations with CCM and TCM are compared

131   in Section 4.2.

132   The unsteady RANS model is used for the transient simulations with both CFD codes. In

133   OpenFOAM, the RNG (Re-Normalisation Group) k–ε model (Yakhot et al., 1992) is

134   deployed for turbulence closure. All transport equations are discretized using the total

135   variation diminishing (TVD) scheme (Harten, 1984; Yee, 1987), which combines the

136   first-order upwind difference scheme and the second-order central difference scheme. The

137   PIMPLE algorithm, a merged PISO (Pressure Implicit with Splitting of Operator)–

138   SIMPLE (Semi-Implicit Method for Pressure-Linked Equations) algorithm in the

139   OpenFOAM toolkit, is used for pressure–velocity coupling. In Code_Saturne, turbulence

140   is solved using the k–ε turbulence model (linear production) (Guimet and Laurence, 2002).

141   The time and space discretizations of velocity, pressure and other scalars in all transport

142   equations are realized through a centred scheme and a fractional step scheme

143   (Archambeau et al., 2004) . For both CFD software, the dry deposition schemes for gas

144   and particle are added to the transport equations using volume sink terms based on Zhang

145   et al. (2003) and Zhang et al. (2001), respectively. The details of the implementation are
146   provided in Appendix A.
147   SSH-Aerosol (Sartelet et al., 2020) is a modular box model that simulates the evolution
148   of not only gas concentrations but also the mass and number concentrations of primary
149   and secondary particles. In SSH-Aerosol 112 gas species and 40 particle species are
150   considered. The particle compounds are dust, black carbon, inorganics (sodium, sulphate,
151   ammonium, nitrate and chloride), primary organic aerosol (POA) and secondary organic
152   aerosol (SOA). Three main processes involved in aerosol dynamics (coagulation,
153   condensation /evaporation and nucleation) are included. The particle size distribution is
154   modelled using a sectional size distribution. Nucleation is not considered in this study
155   because only the mass and not the number of particles is available for evaluation, and
156   large uncertainties remain on the nucleation parameterizations (Sartelet et al., 2022)
157   mostly affecting the number of particles. As nucleation is not considered, the minimum
158   diameter does not need to be as low as 0.001 μm, and it is fixed to 0.01 μm, as in the
159   regional-scale simulations of Sartelet et al. (2018), which provide the background
160   concentrations. Six particle size sections are employed with bound diameters of 0.01, 0.04,
161   0.16, 0.4, 1.0, 2.5 and 10 μm.
162   The coupling between CFD and SSH-aerosol are achieved by using the application
163   program interface (API) of SSH-aerosol. The gas and particle concentrations are
164   initialized in CFD and are transported in the domain for each time step. For each grid
165   volume cell, these transported concentrations, as well as meteorological parameters, such
166   as temperature and humidity, are then sent to SSH-aerosol to advance one time step of
167   gaseous chemistry and aerosol dynamics. Once the SSH-aerosol calculation is completed,
168   the concentrations are sent back to the CFD for the next time step. It should be noted that
169   as the SSH-aerosol processes the ensemble-averaged concentration from RANS model,
170   the covariance of turbulent diffusion and chemical reaction may not be fully reproduced.
171   The influence of different operator splitting algorithms is discussed in Section 4.4.
172

3. Simulation setup
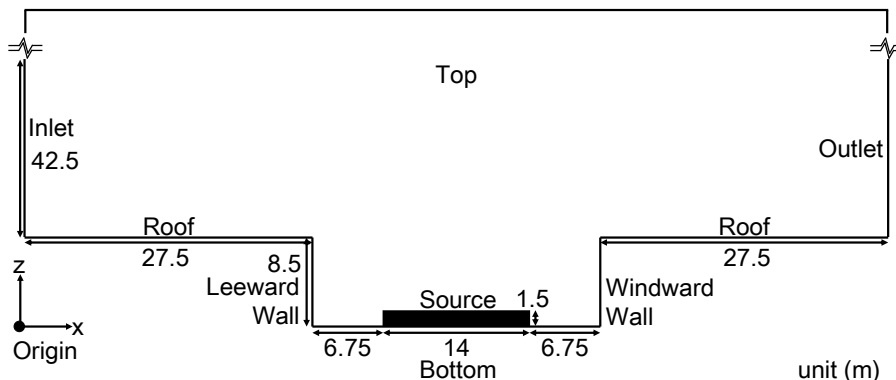
Fig. 1 Simulation domain of street canyon

The simulation is set up to model a street in Greater Paris (Boulevard Alsace-Lorraine), where field measurements were conducted from April 6 to June 15, 2014. The concentrations of nitrogen dioxide (NO_2), particles with diameters less than 10 µm (PM_{10}), and black carbon were measured as described in (Kim et al., 2018). Fig. 1 shows the simulation domain. The 2-D street canyon is 27.5 m in width (W) and 8.5 m in height (H). The domain height is 6 H. The street canyon is discretized into uniform grids in x- and z- directions. The grid resolutions in the street canyon are 0.5 m in both x-and z- directions, respectively. The largest grid sizes are 4 m (x) × 2m (z). An analysis of the grid sensitivity is described in Section 4.3.

Simulations are conducted from 4:30 a.m. to 5 p.m. on April 30, 2014 at local time (GMT+2). This period is selected because the wind direction is almost perpendicular to the street canyon during that day, allowing for a 2D simulation setting. During the field measurement, there exists several time periods that the wind direction is perpendicular with the street canyon. Meanwhile, some time periods are short (less than 5 hours), and we consider that short period simulation is not representative in simulation accuracy. In addition, we consider that it is critical to have a simulation time long enough to cover both day-time chemistry and night-time chemistry. The first 30 minutes of the simulation corresponds to model spin-up, and the simulation lasts 12 hours. A sensitivity analysis of numerical aspects, such as the splitting method between transport and chemistry and the time step, is described in Section 4.4.
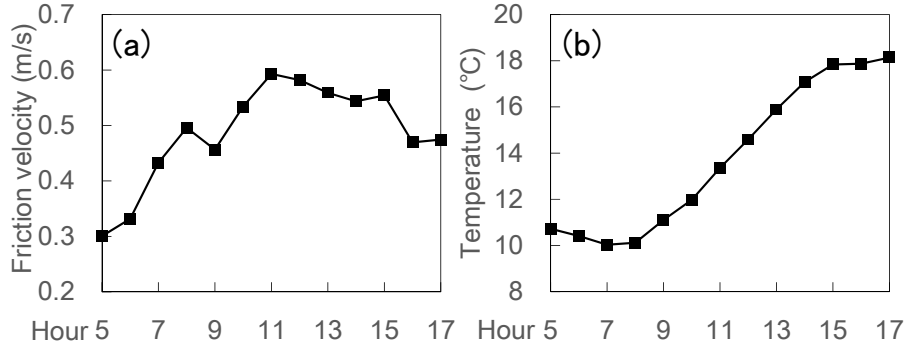
Fig. 2 Time variations of hourly friction velocity and temperature for inflow.

Meteorological conditions (Fig. 2) including time-varying friction velocity and temperature are obtained from the simulation described in Sartelet et al. (2018) using the Weather Research and Forecasting (WRF) model. The grid resolution is 1 km ×1 km in Paris. The lowest and highest friction velocities occurred approximately at 5 a.m. and 11 a.m., respectively. The lowest and highest temperatures are around 8 a.m. and 5 p.m. For the inflow, the wind direction is perpendicular to the street canyon. The friction velocity u_* is used to prescribe the vertical profiles of the streamwise velocity U, turbulent kinetic energy k and turbulent dissipation rate ε as follows

$$U(z) = \frac{u_*}{\kappa} \ln \left(\frac{z - H}{z_0} \right) \tag{1}$$

$$k(z) = \frac{u_*^2}{\sqrt{C_\mu}} \tag{2}$$

$$\varepsilon(z) = \frac{u_*^3}{\kappa(z - H)} \tag{3}$$

where κ is the von Kármán constant and C_μ is the model constant (=0.09) in the k-ε model. The roughness length z_0 is set to 1 m for the inlet (Belcher, 2005) and 0.1 m for the wall and bottom (Lo and Ngan, 2015).
In addition, since the domain height is low (51 m) in this study and we focus on the pollutant dispersion behaviors in the street canyon, it is reasonable to consider the atmospheric stability as neutral; therefore the temperature is assumed to be spatially uniform at the inflow. The hourly friction velocities and temperatures are linearly interpolated into each timestep and prescribed at the inflow. It should be noted that the general trends are simulated but the fast fluctuations at the inlet are not reproduced. The same linear interpolation is used for background concentrations and emission rates, which will be described in the following.
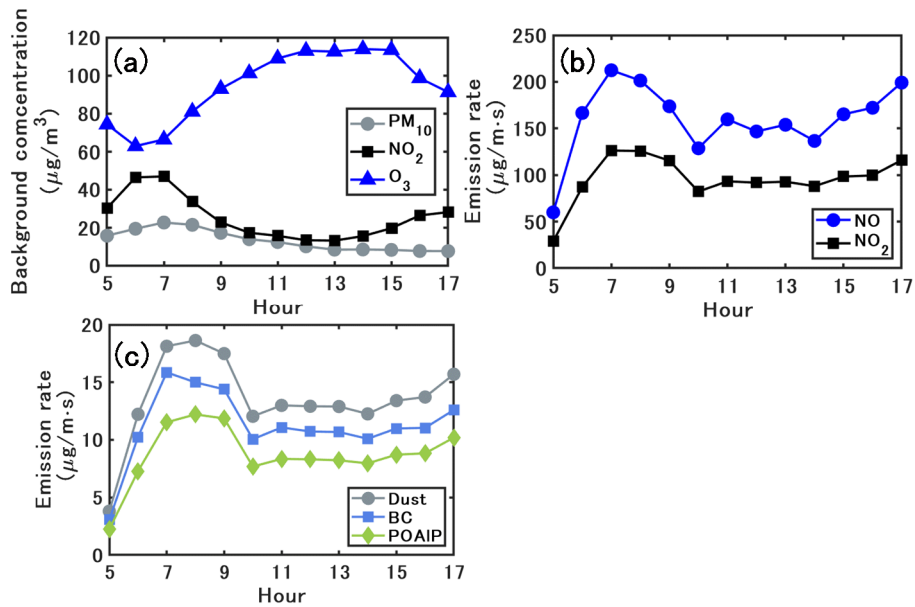
Fig. 3 Time variations of (a) PM_{10}, NO and NO_2 background concentrations, (b) emission rates of NO and NO_2 and (c) emission rates of dust, BC and organics (POAlP).

Fig. 3(a) shows the time variations of the PM_{10}, NO and NO_2 background concentrations. Fig. 3(b) and (c) show the emission rates for NO, NO_2 and the emitted compounds of PM_{10}. The background concentrations of the gas and particles are obtained from the regional-scale simulations of Sartelet et al. (2018) with the Eulerian model Polair3D of the Polyphemus air quality modelling platform (Mallet et al., 2007), which uses the same chemical representation as in this study. As detailed in Sartelet et al. (2018), the regional background concentrations compare well to measurements of O_3, NO_2, PM_{10}, $PM_{2.5}$, black carbon and organic aerosols. The hourly background concentrations are linearly interpolated into each timestep and spatial-uniformly prescribed at the inflow and top. The traffic emission source is assumed to be approximately 14 m in width and 1.5 m in height, and it is set in the middle of the bottom of the canyon (Fig. 1). As detailed in Kim et al. (2022), emissions are estimated from the fleet composition and the number of vehicles in the street using COPERT's emission factors (COmputer Program to calculate Emissions from Road Transport, version 2019, EMEP/EEA, 2019). After the speciation of NO_x, Volatile Organic Compounds (VOC), $PM_{2.5}$ and PM_{10} into model species, emissions are set for 16 gaseous model species and three particle model species: dust and unspecified matter (Dust), black carbon (BC) and primary organic aerosol of low volatility (POAlP). The PM size distribution at emission is assumed to be the same as in the previous studies (Lugon et al., 2021a, 2021b). The exhaust primary PM is assumed to be in the size bin [0.04 – 0.16 μm] while non-exhaust primary PM is coarser in the size

244   bin [0.4 – 10 μm].

245   For the boundary conditions of the OpenFOAM, the pressure and the gradients of all other

246   variables are set to zero at the outlet. For the walls, we use the wall functions of ε and

247   turbulent kinematic viscosity ν_t for atmospheric boundary layer modelling in

248   OpenFOAM toolkit (OpenFOAM user guide) based on (Parente et al., 2011). The

249   gradients of turbulent kinetic energy k, concentration, and temperature are set to zero. In

250   Code_Saturne, a two-scales logarithmic friction velocity wall function is used for solving

251   the fluid velocity near wall cell and a three layers wall function is used for computing

252   other transported scalar profiles such as temperature near the wall (Arpaci and Larsen,

253   1984).

254   The turbulent Schmidt number Sc_t in the concentration transport equations, which is the

255   ratio of the turbulent diffusivity to the concentration and turbulent kinematic viscosity, is

256   important in turbulent diffusion modeling. The value of Sc_t is considered between 0.2

257   and 1.3, depending on the flow properties and geometries (Tominaga and Stathopoulos,

258   2007). For urban environments with a compact layout, a small $Sc_t = 0.4$ is found to

259   show better agreement with wind tunnel experiment data (Di Sabatino et al., 2007).

260   Therefore, a value of 0.4 is adopted in the current study.

261

262   **4. Model evaluation**

263   *4.1. Validation with field measurements and comparison of simulated concentrations with*

264   *the two CFD software*
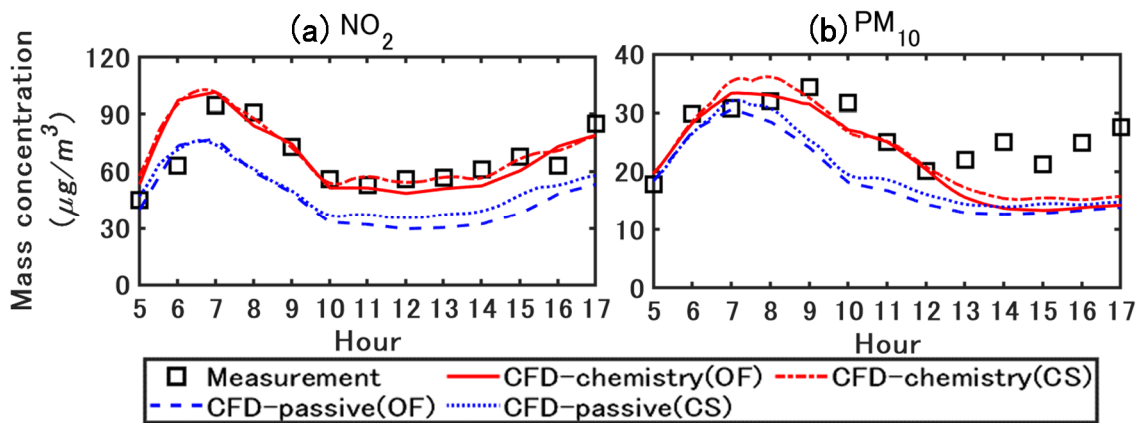
265

266   Fig. 4 Measured and simulated NO_2 and PM_{10} concentrations. The values are spatially

267   averaged in the street canyon ($27.5 \leq x \leq 55, 0 \leq z \leq 8.5$ m). CFD-passive and CFD-

268   chemistry denote the CFD simulation without and with chemistry coupling. OF and CS

269   denote the simulated concentrations based on OpenFOAM and Code_Saturne. All

270   concentrations are represented in local time (GMT+2).

271

9

272   Reproducing the flow field is important in this study. Meanwhile, the observation data on
273   wind velocity is not available. Therefore, we conducted a velocity validation for
274   OpenFOAM v2012 using data from a wind tunnel experiment (Blackman et al., 2015).
275   The predicted mean velocity agreed well with the experimental values. The details can be
276   found at Appendix B.

277   Fig. 4 compares the simulated concentrations with those obtained from the field
278   measurements. In the field measurements, the measured concentration was obtained from
279   averaging over two measurement points near the leeward and windward walls in the street
280   canyon. In this section, the simulated results and discussion are based on the spatially-
281   averaged values in the street canyon ($27.5 \leq x \leq 55, 0 \leq z \leq 8.5$ m). CFD-passive and
282   CFD-chemistry denote the CFD simulation without and with chemistry coupling. OF and
283   CS denote simulated concentrations based on OpenFOAM and Code_Saturne. The
284   operator splitting order and time step for OF and CS are the A-B-A splitting method with
285   0.5 s and the A-B splitting method with 0.25 s, as detailed in Section 4.4. The simulation
286   time ratio of CFD-chemistry and CFD-passive is about three times in both OpenFOAM
287   and Code_Saturne in this study.

288   For NO_2, the peak concentration in the field measurement occurred approximately at 7
289   a.m. owing to the morning traffic. In the CFD-passive simulations, the lack of chemical
290   reactions lead to an underestimation of NO_2, while the concentrations simulated with
291   CFD-chemistry agree well with the measurements. For PM_{10}, the concentrations
292   simulated with CFD-chemistry also show better agreement with the measurements than
293   CFD-passive. The primary reason is that CFD-chemistry can reproduce the condensation
294   of inorganic and organic matter from the gas phase to the particle phase, which will be
295   further explained in the following sections. The simulation results based on OF and CS
296   show small differences, and detailed comparisons are presented in Fig. 6.

297   Validation metrics (Chang and Hanna, 2004) are used to quantify the overall accuracy of
298   the CFD simulated concentrations based on OF, compared with the measured values
299   (Trini Castelli et al., 2018; Ferrero et al., 2019). The following metrics are used: fractional
300   bias (FB), geometric mean bias (MG) and normalized mean square error (NMSE). These
301   metrics are defined as follows:

$$\text{FB} = \frac{\overline{Obs} - \overline{CFD}}{0.5\left(\overline{Obs} + \overline{CFD}\right)} \tag{4}$$

$$\text{MG} = \exp\left(\overline{\ln Obs} - \overline{\ln CFD}\right) \tag{5}$$

$$\text{NMSE} = \frac{\overline{(Obs_i - CFD_i)^2}}{\overline{Obs} \times \overline{CFD}} \tag{6}$$

302   where Obs_i and CFD_i are the measured and CFD simulated concentrations for the

303 compound/species i, respectively. The overbar represents the mean value of the entire

304 dataset. The ideal values are 1 for MG, and 0 for FB and NMSE. Previous research has

305 suggested that $|FB| < 0.3$, $0.7 < MG < 1.3$ and $NMSE < 4$ are acceptable for

306 simulated concentrations (Hanna et al., 2004).

307 Table 1 shows the statistical indicators for spatially averaged concentrations of NO_2 and

308 PM_{10} in the street canyon from 5 a.m. to 5 p.m. For NO_2 and PM_{10}, the mean and 90%

309 percentile concentrations simulated with CFD-chemistry are closer to the measurements

310 than those simulated with CFD-passive. In addition, the FB, MG and NMSE values of

311 CFD-chemistry are closer to the ideal values than those of CFD-passive.

312

313 Table 1 Statistical indicators for NO_2 and PM_{10} in the street canyon from 5 a.m. to 5p.m.

314 The concentrations are simulated with OpenFOAM.

|	Concentration ($\mu g/m^3$)		Validation metrics		
NO_2	Mean	Percentile 90%	FB	MG	NMSE
Measurement	66.6	91.8	/	/	/
CFD-chemistry	67.3	97.3	-0.01	1.00	1E-4
CFD-passive	45.9	73.7	0.36	1.50	0.14
PM_{10}	Mean	Percentile 90%	FB	MG	NMSE
Measurement	26.4	32.5	/	/	/
CFD-chemistry	22.3	33.1	0.17	1.23	0.03
CFD-passive	18.8	28.9	0.34	1.45	0.13

315
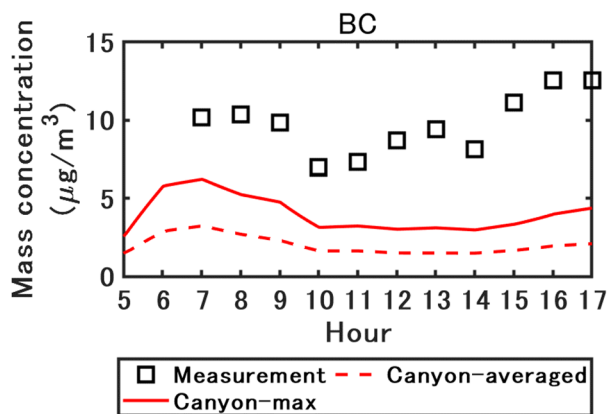
316

317 Fig. 5 Measured and simulated black carbon concentrations with OpenFOAM. The

318 canyon-averaged and maximum concentrations in the street canyon are represented by

319 the plain line and the dashed line respectively ($27.5 \leq x \leq 55, 0 \leq z \leq 8.5$ m).

320

321 The black carbon (BC) concentration simulated with OF is compared with the
322 measurements in Fig. 5. Because BC is considered an inert matter, considering chemistry
323 does not influence the mass concentration. Therefore, the concentrations simulated with
324 CFD-passive and CFD-chemistry show little difference; only the concentration simulated
325 with CFD-chemistry is shown here. The BC concentrations are underestimated by a factor
326 of approximately 5. Even the maximum concentrations in the street canyon largely
327 underestimate the measurements. One of the causes of this underestimation may be the
328 underestimation of the non-exhaust tyre emission factors in the COPERT emission factors
329 used here (Lugon et al., 2021a).
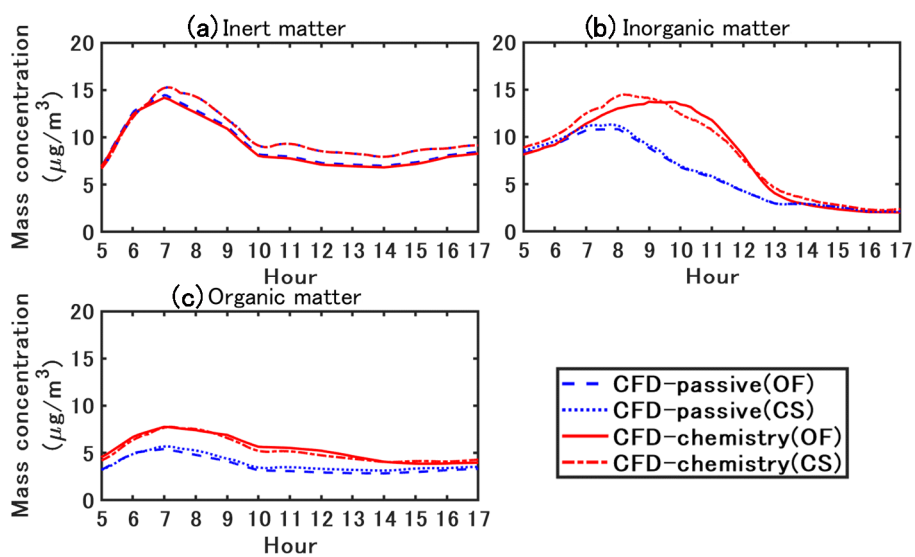
330
331 Fig. 6 Simulated particle concentrations with OpenFOAM (OF) and Code_Saturne (CS).
332 CFD-passive and CFD-chemistry denote the CFD simulation without and with chemistry
333 coupling.
334
335 The particle concentrations simulated with OF and CS are compared in Fig. 6. The
336 evolutions of the concentrations simulated by OF and CS are similar. Higher PM_{10}
337 concentrations are simulated by CS around 8 a.m. during the traffic peak and in the
338 afternoon, mostly because of the higher concentrations of emitted inert compounds, such
339 as black carbon and dust. Differences in the turbulence scheme may explain these
340 variations. Meanwhile, the difference between CFD-passive and CFD-chemistry for the
341 inorganic and organic matter is in accordance with OF and CS, showing the robustness
342 of the coupling method between CFD and SSH-aerosol by API. For simplicity, only the
343 simulated concentration based on OF is presented and discussed in the following sections.
344

345 *4.2. Transient-condition method and constant-condition method*
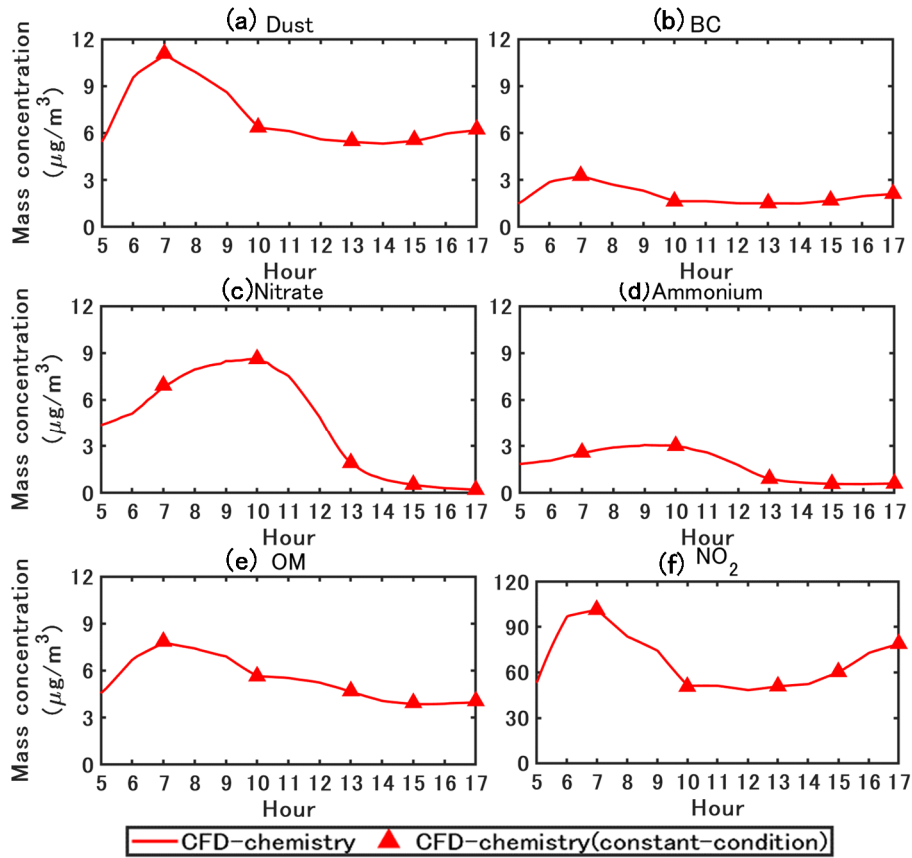
346
347 Fig. 7 Simulated PM$_{10}$ and NO$_2$ concentrations with the transient-condition and constant-
348 condition methods. The concentrations are spatially averaged in the street canyon.
349
350 To validate the simulation accuracy of CCM in simulations that consider both gas
351 chemistry and particle dynamics, simulations are conducted using boundary conditions
352 and emission rates at five time points (7 a.m., 10 a.m., 1 p.m., 3 p.m. and 5 p.m.). Other
353 simulation conditions, including the grid, coupling method, and time step, are the same
354 as the transient-condition simulation.
355 In Fig. 7, for PM$_{10}$ and NO$_2$, the concentrations simulated with CCM (red triangles) are
356 similar to those simulated with TCM. In addition, depending on the background
357 concentration and emission conditions, the simulation time required for CCM to reach
358 dynamic equilibrium is less than 1000 time steps (approximately 500 s). Therefore, CCM
359 can be utilized for parameter studies. The sensitivity analysis of the grid, coupling method
360 and time step in Section 4.3 and 4.4 is based on CCM. However, CCM should be used
361 with caution when the inflow wind speed and direction vary rapidly. The simulated
362 concentrations in Section 5 are based on TCM.
363

364   *4.3. Grid sensitivity*
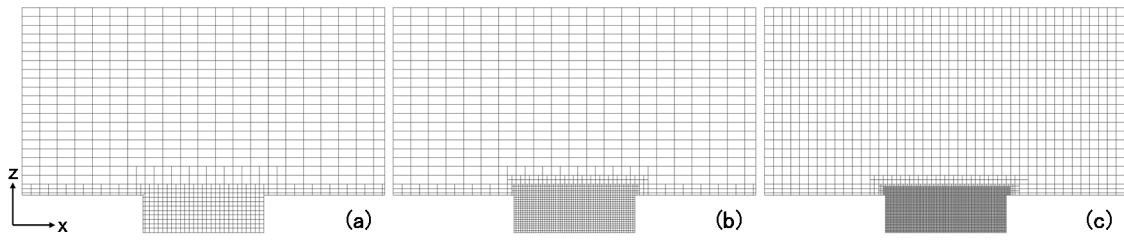
365

366   Fig. 8 Different grid resolutions for sensitivity analysis: (a) coarse, (b) basic, (c) fine. The
367   grid resolutions in the street canyon are 1 m, 0.5 m and 0.25 m in both x-and z- directions,
368   respectively. The largest grid sizes are 4 m (x) × 2m (z) in the coarse and basic grids,
369   and 2 m (x) × 2m (z) in the fine grid.

370

371   Grid sensitivity analysis is conducted based on three different resolutions as shown in Fig.
372   8. The grid resolutions in the street canyon for coarse, basic and fine grids are 1 m, 0.5 m
373   and 0.25 m in both x-and z- directions, respectively. The largest grid sizes are 4 m (x) ×
374   2m (z) for the coarse and basic grids, and 2 m (x) × 2m (z) for the fine grid. The
375   simulations are based on constant-condition method. The A-B-A splitting method, which
376   is introduced in Section 4.4, is used with a time step of 0.5 s. Fig. 9 shows the comparative
377   results for the mass concentration. No significant discrepancy is observed between the
378   different grids for NO_2, inert matter and organic matter. Meanwhile, the simulated
379   inorganic matter based on coarse grids shows slightly smaller concentrations than the
380   other grid resolutions, while the concentrations based on basic and fine grids are close.
381   Therefore, the basic grid is adopted for simulations in this study.
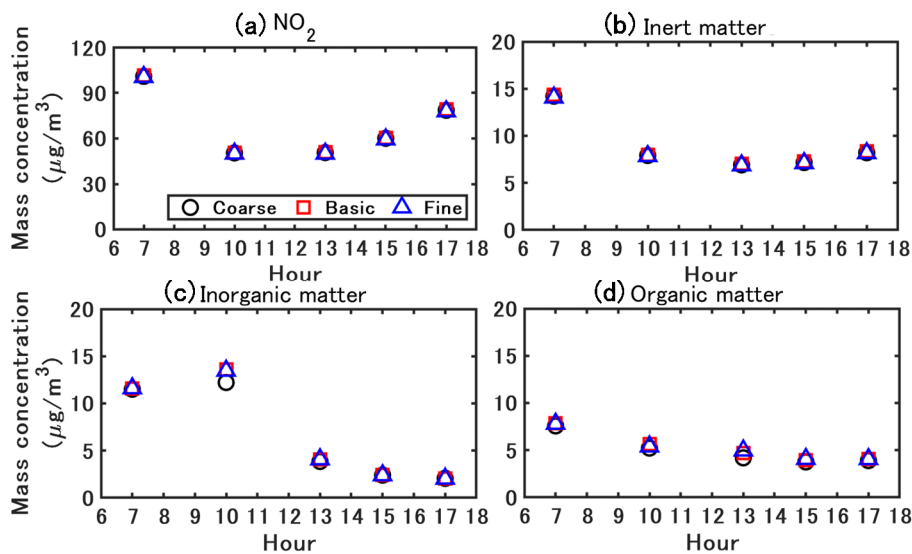
382

383   Fig. 9 Simulated NO_2 and particle concentrations with different grid resolutions.

384

4.4. Coupling method and time step sensitivity

The transport equation for the chemical species includes terms of advection, diffusion, emission and chemical reactions. Ideally, the transport equation should be solved with all the above terms, that is, by coupling all processes. However, the chemical process is integrated with a stiff integrator, whereas advection, diffusion and emission are integrated with a flux scheme. Therefore, operator splitting (Sportisse, 2000) is often employed to solve different terms individually and sequentially over a given time step in chemical transport simulations (Fu and Liang, 2016).

In this study, advection, diffusion and emission are simultaneously solved in CFD, and the chemical reactions including gas chemistry, particle dynamics and size redistribution are solved in SSH-Aerosol. Two operator-splitting orders are considered for coupling: A-B splitting and A-B-A splitting (Sportisse, 2000). For A-B splitting, which can be summarized as CFD(Δt)-Chemistry(Δt), the mass concentrations are first integrated for transport over a time step Δt. The updated concentrations are then integrated for chemistry at the same Δt. On the other side, A-B-A splitting adopts a symmetric sequence of operators, which can be summarized as CFD($\Delta t/2$)-Chemistry(Δt)-CFD($\Delta t/2$). The mass concentrations are first integrated for transport over a half time step, then for chemistry over the full time step and finally for transport again over a half time step.

Table 2 Relative change in the computation time with different operator-splitting order and time steps. The computation time is normalized by ABA-05.

Case	Operator splitting order	Δt (s)	Change in the computation time
AB-05	A-B splitting CFD(Δt)-Chemistry(Δt)	0.5	0.90
AB-025		0.25	1.56
ABA-1	A-B-A splitting CFD($\Delta t/2$)-Chemistry(Δt)-CFD($\Delta t/2$)	1	0.57
ABA-05		0.5	1
ABA-025		0.25	2.44

A sensitivity analysis is conducted on the operator splitting method and splitting time step. As shown in Table 2, the time step is considered 0.5 s and 0.25 s for the A-B splitting (named AB-05 and AB-025), and 1 s, 0.5 s and 0.25 s for the A-B-A splitting (named ABA-1, ABA-05 and ABA-025). The simulated NO_2 and particle concentrations are presented in Fig. 10. ABA-1 and AB-05 concentrations hardly differ from the figures. Meanwhile, the computational time of ABA-1 is only 63% of that of AB-05. Similarly, the concentrations simulated with ABA-05 and AB-025 are almost the same, and the

414   computational time of ABA-05 is only 64% of AB-025. Therefore, the A-B-A splitting

415   method can be considered as a cost effective method.

416
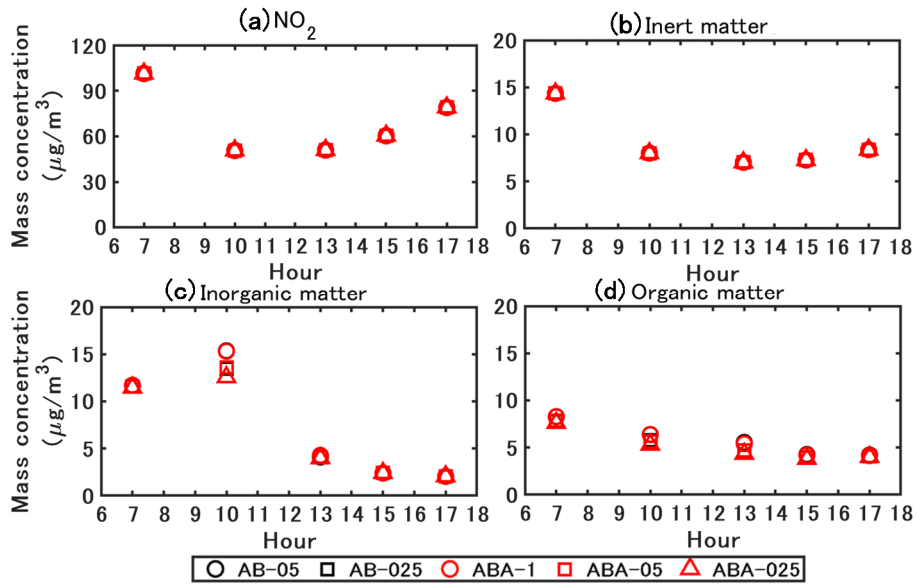
417

418   Fig. 10 Simulated NO_2 and particle concentrations with different coupling methods and

419   time steps. ABA denotes the A-B-A splitting method: CFD($\Delta t/2$)-Chemistry(Δt)-

420   CFD($\Delta t/2$). AB denotes the A-B splitting method: CFD(Δt)-Chemistry(Δt). In the legend,

421   the values that follow the capital letter ABA or AB denote the time step Δt (in s) used in

422   the simulation.

423

424   The concentrations simulated with the A-B-A splitting method and different time steps

425   show that small time step results in low inorganic and organic matter concentrations. The

426   concentrations simulated with ABA-1 are larger than those of ABA-05, and larger than

427   ABA-025. However, the differences between the concentrations simulated with ABA-05

428   and ABA-025 are lower than the differences between ABA-1 and ABA-05. For NO_2 and

429   inert particles, no obvious difference is found between the simulations with different

430   splitting methods and splitting time steps. Therefore, the A-B-A splitting method with a

431   time step of 0.5 s is adopted in this study.

432

5. Results and discussion

5.1. Time-averaged flow field and concentration field
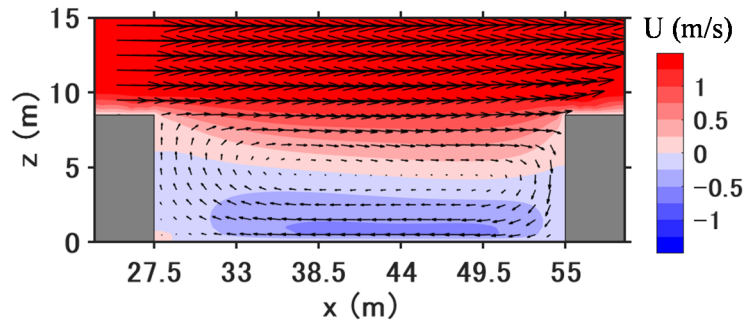
Fig. 11 Time-averaged flow field in the street canyon from 5 a.m. to 5 p.m.

This section shows the results for time-averaged values from 5 a.m. to 5 p.m. Fig. 11 shows the 12-hour time-averaged streamwise velocity and wind direction in the street canyon. At the current aspect ratio (H/W=0.31), a large vortex is observed in the canyon with a small secondary vortex at the corner of the leeward wall. A reverse flow is observed in the lower half of the canyon.
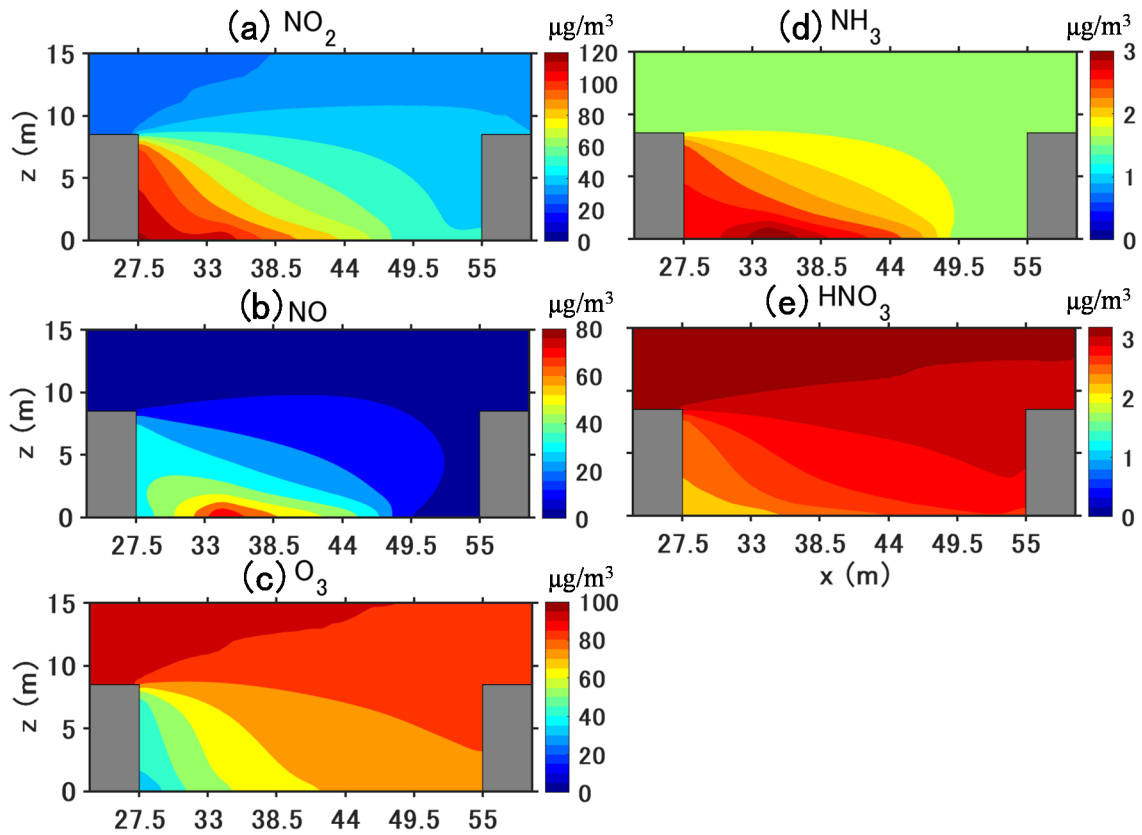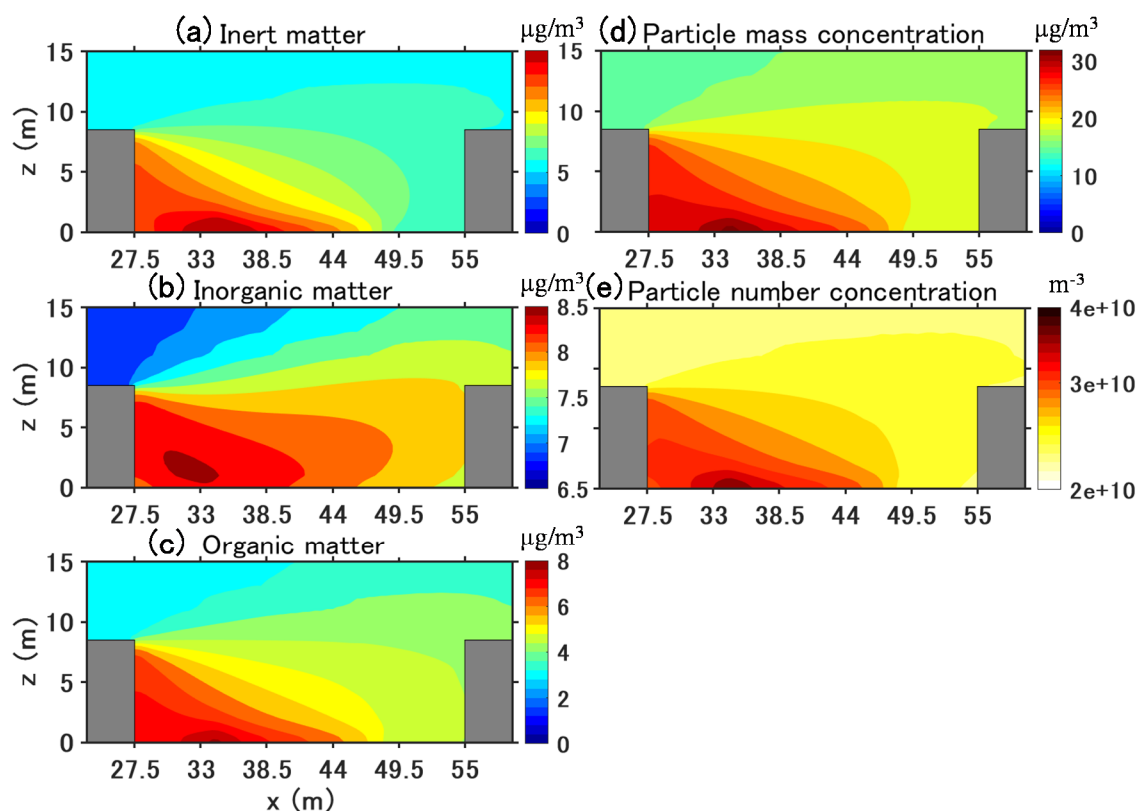

Fig. 12 Time-averaged concentrations ($\mu g/m^3$) of gaseous pollutants in the street canyon

445   from 5 a.m. to 5 p.m.

446

447   Fig. 12 shows the time-averaged concentrations of the gaseous pollutants from 5 a.m. to

448   5 p.m. For gaseous pollutants emitted by traffic, such as NO_2, NO and NH_3, larger

449   concentrations are found in the street, particularly near the leeward wall, compared to the

450   windward wall due to the reverse flow. Simultaneously, gas-phase chemistry and

451   condensation/evaporation between the gas and particle phases also influence the

452   concentration distribution. NO_2 mainly increases due to chemical production from NO

453   emissions and background O_3. Compared to the background NO_2 concentration of 26

454    $\mu g/m^3$, the longest retention time at the leeward side corner leads to the street canyon's

455   largest concentration (121 $\mu g/m^3$). At pedestrian height (z=1.5 m), NO_2 concentration is

456   116 $\mu g/m^3$ at the leeward wall and 49 $\mu g/m^3$ at the windward wall.

457   However, NO and NH_3 generally decrease because of loss by gaseous chemistry and the

458   condensation of ammonium nitrate, respectively; therefore, the largest concentrations are

459   at the leeward corner of the traffic emission source. For secondary gaseous pollutants

460   without traffic emissions such as O_3 and HNO_3, gaseous chemistry and condensation lead

461   to lower concentrations in the street canyon than background concentrations. For O_3, this

462   is due to the titration of O_3 by NO, whose concentration is large near the leeward wall.

463   For HNO_3, this is because of the high concentrations of NH_3, which then condenses with

464   HNO_3 to form ammonium nitrate. In addition, the lowest concentration of O_3 and HNO_3

465   can be found at the leeward corner which corresponds to the secondary vortex in Fig. 11,

466   indicating that the pollutant residence time is the highest in that corner leading to enhance

467   ozone titration.

Fig. 13 Time-averaged concentrations of particle number, mass and composition in the street canyon from 5 a.m. to 5 p.m. The unit is μg/m³ for mass concentration and m⁻³ for number concentration.

Fig. 13 shows the time-averaged PM_{10} mass concentration, and the number concentrations and PM composition (inorganic, organic and inert matter) from 5 a.m. to 5 p.m. For inert and organic matter, the highest concentrations are near the leeward corner of the traffic emission source. Because inorganic matter is not emitted, the concentration distribution differs from inert and organic matter. However, as they are produced from gas condensation and strongly influenced by traffic emissions, the highest concentrations are observed in the leeward corner.

At pedestrian height (z=1.5 m), the PM_{10} mass concentration is approximately 28 μg/m³ at the leeward wall and 19 μg/m³ at the windward wall, which is larger than the background concentration of 15 μg/m³. The number concentration is computed from the mass concentration and therefore has a similar spatial distribution as PM_{10} mass concentration (nucleation from gas was not taken into account). Traffic emission significantly increases the number concentration. The number concentration is about 2.3×10^{10} m^{-3} in the background, whereas the largest number concentration in the street canyon is about 3.8×10^{10} m^{-3}.

5.2. Time-variant characteristics
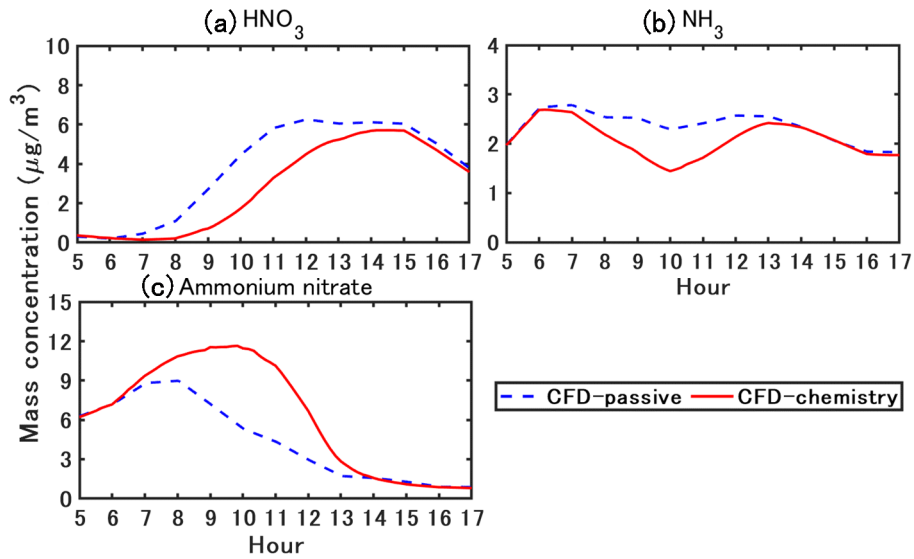

490

491   Fig. 14 Simulated time-varying concentrations of ammonium nitrate and precursor gas

492   (HNO_3 and NH_3).

493

494   Fig. 14 shows the simulated time-varying concentrations of ammonium nitrate formed by

495   the condensation of HNO_3 and NH_3. Based on the traffic fleet in the current study, NH_3

496   emission is approximately 1-2% of NOx emissions. Ammonium nitrate and HNO_3 are not

497   emitted and differences between simulations with or without chemistry coupling are due

498   to gas chemical reactions and phase change between the gas and particle. Phase change

499   may be driven by NH_3 emissions, as well as the non-thermodynamic equilibrium of the

500   background concentrations.

501   In CFD-passive, NH_3 concentration peaks around 7 a.m. as NOx because it is emitted by

502   traffic. The peak in HNO_3 concentration is later in the morning, around 11 am. HNO_3 is

503   formed from the oxidation of NO_2, which is emitted by traffic and is rapidly formed from

504   NO traffic emissions. The formation of HNO_3 is slower than the formation of NO_2, and

505   probably occurs at the regional scale, leading to a delay in the peak of HNO_3

506   concentration compared to NO_2 concentration. In CFD-chemistry, the temporal variations

507   of HNO_3 concentration show large differences with CFD-passive because HNO_3

508   condenses with NH_3 to form ammonium nitrate during the daytime. As a result, the HNO_3

509   concentration peak in CFD-chemistry is later than that in CFD-passive (it is shifted from

510   11 a.m. to around 2 p.m.). The NH_3 concentration in CFD-passive peaks at 7 a.m. because

511   of traffic emission and is stable from 7 a.m. to 1 p.m. and then decreases from 1 p.m.

512   Meanwhile, the condensation in CFD-chemistry leads to lower concentration than in

513   CFD-passive during the daytime (between 7 a.m. and 1 p.m.).

514   For 12-hour time-averaged concentrations, ammonium nitrate increases by 46% in CFD-

515   chemistry compared with that in CFD-passive. Background ammonium nitrate

516   concentration (CFD-passive) peaks around the morning rush (7 to 8 a.m.) and then

517   decreases. Meanwhile, in CFD-chemistry, ammonium nitrate concentration peaks later

518   around 10 a.m., because of the large increase in HNO_3 between the traffic rush and 10

519   a.m. However, although HNO_3 concentration does not vary much between 11 a.m. and 3

520   p.m., the ammonium nitrate concentration decreases from 10 a.m. to a very small level

521   (lower than 1 µg/m^3) after 2 p.m. This decrease is probably linked to the temperature

522   increase during the daytime (Fig. 2(b)) and the relative humidity decrease, leading to a

523   decrease in the condensation rate (Stelson and Seinfeld, 1982).
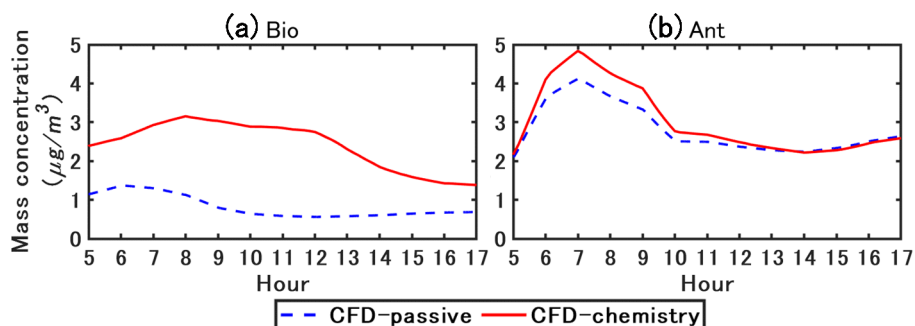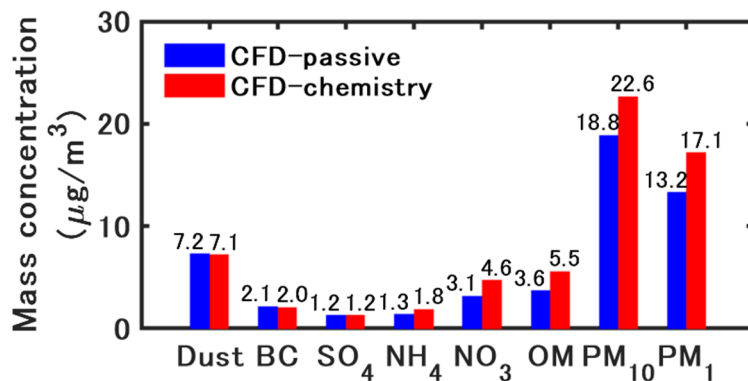

524

525   Fig. 15 Simulated time-varying concentration of organic matter. Bio refers to organic

526   matter formed from biogenic precursors. Ant refers to organic matter formed from

527   anthropogenic precursors.

528

529   Fig. 15 shows the simulated time-varying concentrations of organic matter. Organic

530   matter is divided into two main categories depending on the origin of the precursors: Bio

531   and Ant refer to the organic matter of biogenic and anthropogenic precursors respectively.

532   In CFD-chemistry, Bio concentration is larger than that in CFD-passive. As biogenic

533   precursors are not emitted in the street, the condensation of Bio is due to background

534   precursor gases. As discussed previously, the concentration of ammonium nitrate is higher

535   in CFD-chemistry than in CFD-passive, providing a larger aqueous mass onto which

536   hydrophilic compounds of the biogenic precursor gases condense. As the condensation of

537   ammonium nitrate decreases in the afternoon as shown in Fig. 14, the condensation of

538   Bio also decreases.

539   Ant is largely influenced by traffic emissions in the street, particularly by emissions of

540   semi-volatile compounds (Sartelet et al., 2018), which soon condenses after emissions.

541   Therefore there is a peak around 7 a.m. owing to the morning rush. In the model,

542   anthropogenic emissions are mostly hydrophobic, therefore the condensation is not

543 enhanced by the increase in inorganic concentrations. Consequently, the difference
544 between CFD-chemistry and CFD-passive is larger in the morning owing to the large
545 increase in traffic emissions, but small differences are observed in the afternoon.

546

Fig. 16 Time-averaged concentration of PM_{10}, PM_1 and the chemical compounds of PM_{10} from 5 a.m. to 5 p.m.

547 Fig. 16 Time-averaged concentration of PM_{10}, PM_1 and the chemical compounds of PM_{10}
548 from 5 a.m. to 5 p.m.
549
550 Fig. 16 shows the time-averaged concentrations of PM_{10}, PM_1 and the chemical
551 compounds of PM_{10} from 5 a.m. to 5 p.m. The time-averaged PM_{10} and PM_1
552 concentrations increase by approximately 3.8 $\mu g/m^3$ in CFD-chemistry compared to CFD-
553 passive, indicating that chemistry mainly influences small particles. Inert matter slightly
554 decreases in CFD-chemistry owing to dry deposition. Condensation increases of 48%,
555 38% and 53% of nitrate, ammonium and organic matter concentrations in CFD-chemistry
556 compared to CFD-passive.
557

5.3. Size distribution of particle matter

559
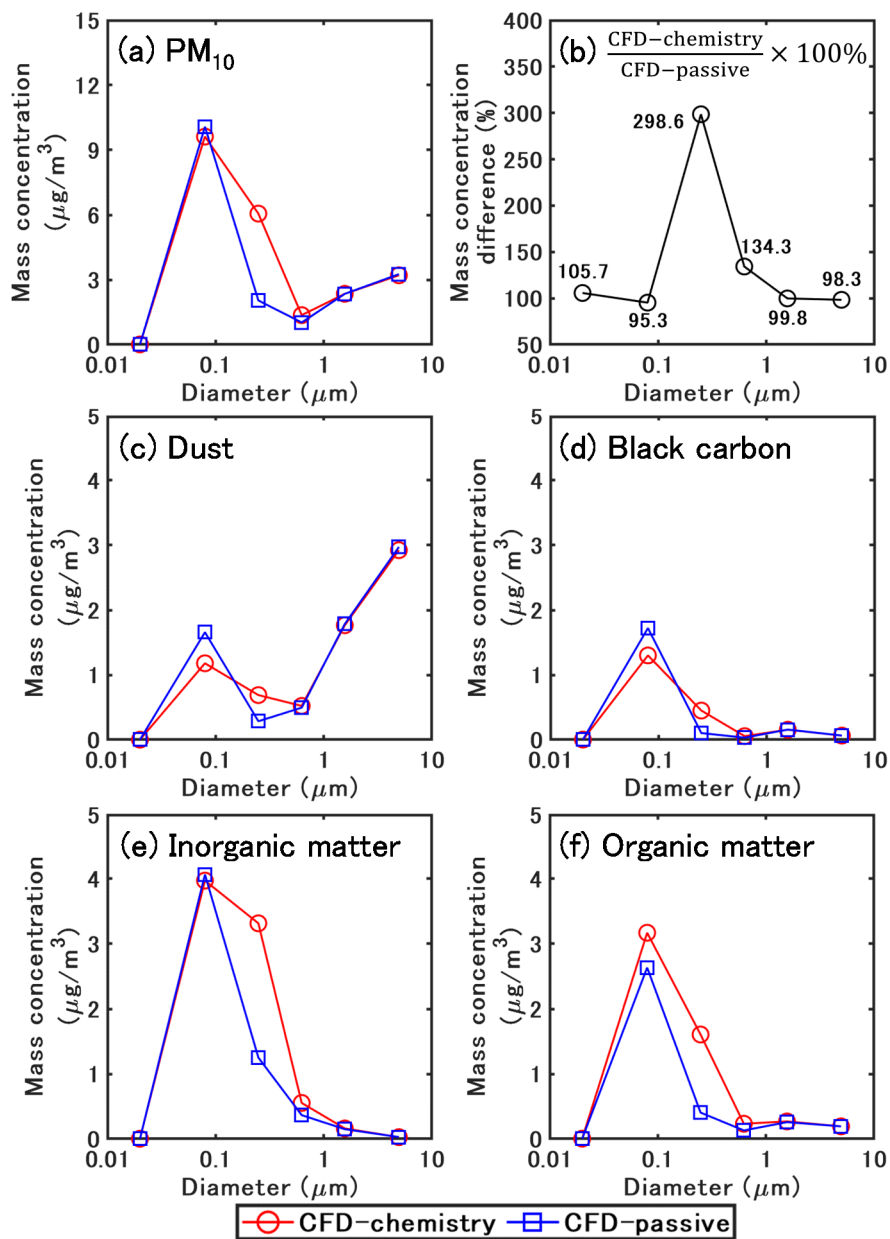
Fig. 17 Time-averaged size distribution of PM_{10} for different chemical species from 5 a.m.

to 5 p.m.

Fig. 17 shows the time-averaged size distribution of PM_{10} for the different chemical

compounds of particles from 5 a.m. to 5 p.m. The bound diameters are 0.01, 0.04, 0.16,

0.4, 1.0, 2.5 and 10 μm, and the mean diameters are 0.02, 0.08, 0.25, 0.63, 1.58 and 5.01

μm.

For the total concentration of PM_{10} (Fig. 17(a)), the lowest and the largest concentrations

are in the first size section (0.01-0.04 μm) and the second size section (0.04-0.16 μm)

569 respectively, for both the CFD-passive and the CFD-chemistry simulations. Generally,
570 the loss and gain of mass concentration in each size section are related to emission, dry
571 deposition, coagulation (small particles coagulate into large particles), and
572 condensation/evaporation (phase exchange between gas and particles).

573 Fig. 17(b) shows the mass concentration ratio between CFD-passive and CFD-chemistry
574 for each size section. For particles in the size range of 0.04-0.16 μm, the concentrations
575 are smaller in CFD-chemistry than in CFD-passive, because dry deposition and
576 coagulation both decrease mass concentration for those particles. Furthermore, semi-
577 volatile gases may evaporate from small particles because of the Kelvin effect and
578 condense onto larger particles. For particles in the size range of 0.16-1.0 μm, the
579 concentrations are much larger in CFD-chemistry than CFD-passive, indicating that
580 coagulation and condensation on the mass-concentration increase are dominant to other
581 processes, such as deposition. For particles larger than 1 μm, the concentrations of CFD-
582 passive and CFD-chemistry are similar, because particle dynamics have a low influence
583 on large particles.

584 The size distribution of dust (Fig. 17(c)) shows that most dust mass concentrations are in
585 particles larger than 1 μm. Meanwhile, most of the mass concentration of BC, inorganic
586 and organic matter (Fig. 17(d-f)) is in particles smaller than 1 μm. Coagulation is the main
587 process influencing the size distribution for inert matter (dust and BC). Compared to
588 CFD-passive, the mass concentration of dust and BC in the second size section decrease
589 by 0.48 and 0.43 μg/m^3 in CFD-chemistry. Correspondingly, the mass concentrations of
590 dust and BC in the third size section increase by 0.41 and 0.35 μg/m^3.

591 For inorganic matter, in the second size section, the concentrations are similar in CFD-
592 passive and CFD-chemistry: particle dynamics decrease sulphate concentration by 0.32
593 μg/m^3 and increase nitrate concentration by 0.17 μg/m^3. However, as the results of the
594 combination effect of coagulation and ammonium nitrate condensation, the
595 concentrations largely increase in the third size section in CFD-chemistry: sulphate,
596 ammonium and nitrate increase by 0.27, 0.6 and 1.24 μg/m^3, respectively.

597 For organic matter, because of condensation of hydrophilic compounds from background
598 biogenic gases and anthropogenic emissions, CFD-chemistry leads to a small increase in
599 concentrations (0.53 μg/m^3) in the second size section and a large increase in the third
600 section (1.21 μg/m^3) compared to CFD-passive. In detail, Bio concentrations increase by
601 0.89 μg/m^3, and Ant concentrations decrease by 0.36 μg/m^3 in the second size section. In
602 the third size section, Bio and Ant concentrations increase by 0.67, 0.54 μg/m^3.

603

5.4. Influence of ammonia traffic emissions
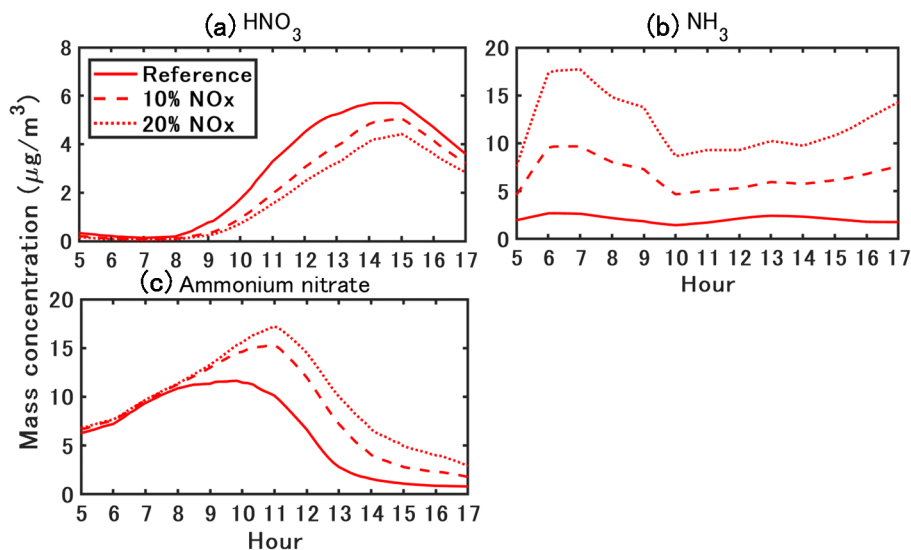
Fig. 18 Sensitivity of ammonium nitrate concentration to NH$_3$ emission.

Suarez-Bertoa et al. (2017) conducted on-road measurements of NH$_3$ emissions from two Euro 6b compliant light duty cars (one gasoline and one diesel) under real-world driving conditions, and they found that NH$_3$ emissions accounted for 11.9% and 0.92% of NOx emissions for gasoline and diesel vehicles. As explained in Section 5.2, NH$_3$ emission emissions are approximately 1-2% of NOx emissions in the reference case. Two cases are considered to simulate the impact of an increase in the fraction of gasoline cars, and sensitivity simulations are performed with NH$_3$ emission considered as 10% and 20% of the NOx emissions.

Fig. 18 shows the sensitivity of ammonium nitrate concentration to NH$_3$ emissions. A larger NH$_3$ emission delays the peak of ammonium nitrate by approximately one hour. For a 12-hour average, considering NH$_3$ emissions of 10% and 20% of NOx emissions leads to a large increase in ammonium nitrate (35% and 55%) compared to the reference case, because of the formation of ammonium nitrate by the condensation of HNO$_3$ and NH$_3$.

6. Conclusions

Particles in urban environment impose adverse impacts on pedestrians' health. Conventional CFD methods regarding particles as passive scalars cannot reproduce the formation of secondary aerosols and may lead to uncertain simulations. Therefore, to increase the simulation accuracy of particle dispersion, we coupled the CFD software OpenFOAM (OF) and Code_Saturne (CS) with SSH-Aerosol, a modular box model to

629   simulate the evolution of primary and secondary aerosols. The main processes involved
630   in the aerosol dynamics (coagulation, condensation /evaporation and dry deposition) were
631   considered.
632   We simulated a 12-hour transient dispersion of pollutants from traffic emissions in a street
633   canyon using the unsteady RANS model. The simulation domain was generated to model
634   a street-canyon where field measurements are available. The flow field was based on the
635   WRF model. The background concentrations of gas and particles were obtained from
636   regional-scale simulations with a chemistry-transport model. The particle diameter range
637   (0.01 μm to 10 μm) was divided into six size sections. The following conclusions were
638   drawn from the results of this study.

639   1) The simulated spatially-averaged values in the street canyon were validated from
640   field measurement using validation metrics. For both OF and CS, the simulated NO_2
641   and PM_{10} concentrations based on the coupling model (CFD-chemistry) achieved
642   better agreement with the measurement data than the conventional CFD simulation
643   which considered pollutants as passive scalars (CFD-passive). The differences
644   between of the OF and CS results were not obvious and were mainly due to the
645   differences in the turbulence scheme. The following conclusions were drawn based
646   on the simulated OF concentrations.

647   2) For the flow field, a large vortex was observed in the canyon with a small secondary
648   vortex at the corner of the leeward wall at the current aspect ratio (H/W=0.31). In
649   CFD-chemistry, because of the reverse flow, the 12-hour (from 5 a.m. to 5 p.m.) time-
650   averaged NO_2 mass concentration, PM_{10} mass and number concentrations at
651   pedestrian height were much higher near the leeward wall (116 μg/m^3, 28 μg/m^3,
652   3.2×10^{10} m^{-3}) than the background (26 μg/m^3, 15 μg/m^3, 2.3×10^{10} m^{-3}).

653   3) Secondary aerosol formation largely affected the mass concentration and size
654   distribution of particle matter. For 12-hour time-averaged concentrations, ammonium
655   nitrate and organic matter increased by 46% and 53% in CFD-chemistry compared
656   to CFD-passive because of condensation of HNO_3 and NH_3, background biogenic
657   precursor-gases and anthropogenic precursor-gas emissions. Coagulation largely
658   influenced the size distribution of small particles by combining particles with a
659   diameter of 0.04-0.16 μm into 0.16-0.4 μm. At the same time, CFD-chemistry
660   showed a much larger concentration than CFD-passive for the particles in 0.16-1.0
661   μm, indicating that the effect of condensation on increasing mass concentration was
662   dominant compared to other chemical processes.

663   4) Urban areas are NH_3-limited (HNO_3 sufficient) areas, therefore, increasing NH_3 leads
664   to a large increase in ammonium nitrate. Vehicles are considered to be the main

665   source of NH_3 in urban environments. Increasing the fleet's proportion of recent

666   gasoline vehicles may increase NH_3 emissions. For a 12-hour average, we considered

667   NH_3 emissions of 10% and 20% of NOx emissions led to a large increase in

668   ammonium nitrate (35% and 55%) compared to the reference case which considers

669   NH_3 emission as 1-2% of NOx emissions.

670   5)   A grid sensitivity analysis showed that the particles' concentrations of inorganic and

671   organic compounds were sensitive to grid resolution, whereas inert particle

672   concentrations were not sensitive to grid resolution. In addition, simulated values

673   based on a grid size of 0.5 m in the street canyon showed small differences with a

674   grid size of 0.25 m, indicating that a spatial resolution of 0.5 m can be enough for

675   reactive particle dispersion at the street level.

676   6)   Operator splitting is often employed to solve the transport term and chemical

677   reactions over a given time step in chemical transport simulations. Two integration

678   orders were considered: A-B splitting method (CFD(Δt)-Chemistry(Δt)) and A-B-A

679   splitting method (CFD($\Delta t/2$)-Chemistry(Δt)-CFD($\Delta t/2$)). The results showed that

680   the A-B-A splitting method had almost the same concentrations as the A-B splitting

681   method with half the computational time. Further sensitivity analysis on the time step

682   showed that a time step of 0.5 s was enough when using the A-B-A splitting method.

683   7)   Conducting a CFD simulation with constant boundary conditions and emission rates

684   at a specific time point is considered a practical method to achieve time-averaged

685   concentrations for evaluating street-level pollutant concentrations. The validation

686   was conducted using conditions on five time points (7 a.m., 10 a.m., 1 p.m., 3 p.m.

687   and 5 p.m.). The simulated concentration based on the above method exhibited

688   almost the same value as the simulation with transient conditions at the same time

689   points.

690 The limitation of this study should be addressed as several reasonable approximations

691 and assumptions were made in the simulation settings.

692   1)   Concerning the simulation domain: since we focused on the coupling of gas chemical

693   reactions and particle dynamics to the CFD codes, we selected a 12-hour period when

694   wind direction was perpendicular to the street. In that case, a 2-D simplification of

695   the simulation domain is reasonable, as shown by Maison et al. (2022). In addition,

696   the 2-D simplification is frequently adopted for studying dispersion of reactive

697   pollutants in a street canyon (Garmory et al., 2009; Wu et al., 2021). However, in

698   more general cases, the pollutant residence time for a 3-D canyon could be shorter

699   compared to the 2-D canyon adopted in this study, and the effects of chemical

700   reaction or aerosol processes could be weaker than this study reported. In addition,

701 various wind directions should be considered to better evaluate the performance of
702 the coupled model. Further work will focus on the application of the coupled model
703 to a complex urban environment with changing wind directions.

704 2) Concerning the physical model: the simulations were based on RANS-closure, and
705 the SSH-aerosol processed the ensemble-averaged concentration, therefore the
706 covariance of turbulent diffusion and chemical reaction may not be fully reproduced.
707 The simulation based on LES may provide better prediction of second-order
708 quantities. In addition, the radiation on the wall may lead street-level-variations of
709 temperature and could affect the flow field and chemical reaction rates. However,
710 this was not considered here, and the radiation effect on the local temperature was
711 simplified as being the same as in the inflow condition. The inflow temperature was
712 obtained from WRF model where the radiation was considered, and the time variation
713 of temperature was considered to be the same as the background.

714 Future work will be conducted on the influence of environmental factors and emission
715 conditions, aiming to provide knowledge to devise suitable countermeasures to decrease
716 particle concentration in microscale urban environments.

717

721

722 Code/Data availability
723 The codes used in this publication are available to the community, and they can be
724 accessed by request to the corresponding author.

725

726 Author contribution
727 KS and RO were responsible for conceptualization. CL, YW, CF, KS, YK and ZW
728 developed the software. CL and YW conduced the visualization and validation; CL, YW
729 and KS performed the formal analysis. KS and RO acquired resources. CL, YW, RO and
730 KS were responsible for writing and original draft preparation. CF, YK, HK reviewed and
731 edited the manuscript All co-authors contributed to the discussion of the paper.

732

733 Competing interests
734 The contact author has declared that neither they nor their co-authors have any
735 competing interests.

736

737 Reference

738 Anenberg, S. C., Miller, J., Minjares, R., Du, L., Henze, D. K., Lacey, F., Malley, C. S.,

739 Emberson, L., Franco, V., Klimont, Z., and Heyes, C.: Impacts and mitigation of excess

740 diesel-related NO x emissions in 11 major vehicle markets, Nature, 545, 467–471,

741 https://doi.org/10.1038/nature22086, 2017.

742 EMEP/EEA: EMEP/EEA air pollutant emission inventory guidebook 2019, EEA Report

743 No 13/2019, European Environment Agency:

744 https://www.eea.europa.eu/publications/emep-eea-guidebook-2019, last access: 14

745 March 2022.

746 Archambeau, F., Méchitoua, N., and Sakiz, M.: Code Saturne: A Finite Volume Code for

747 Turbulent flows - Industrial Applications, International Journal on Finite Volumes, 1,

748 2004.

749 Arpaci, V. S. and Larsen, P. S.: Convection Heat Transfer, Prentice Hall, New York,

750 1984.

751 Belcher, S. E.: Mixing and transport in urban areas, Philosophical Transactions of the

752 Royal Society A: Mathematical, Physical and Engineering Sciences, 363, 2947–2968,

753 https://doi.org/10.1098/rsta.2005.1673, 2005.

754 Bishop, G. A. and Stedman, D. H.: Reactive Nitrogen Species Emission Trends in Three

755 Light-/Medium-Duty United States Fleets, Environ Sci Technol, 49, 11234–11240,

756 https://doi.org/10.1021/acs.est.5b02392, 2015.

757 Blackman, K., Perret, L., and Savory, E.: Effect of upstream flow regime on street

758 canyon flow mean turbulence statistics, Environmental Fluid Mechanics, 15, 823–849,

759 https://doi.org/10.1007/s10652-014-9386-8, 2015.

760 Blocken, B., Tominaga, Y., and Stathopoulos, T.: CFD simulation of micro-scale

761 pollutant dispersion in the built environment, Build Environ, 64, 225–230,

762 https://doi.org/10.1016/j.buildenv.2013.01.001, 2013.

763 Boutahar, J., Lacour, S., Mallet, V., Quelo, D., Roustan, Y., and Sportisse, B.:

764 Development and validation of a fully modular platform for numerical modelling of air

765 pollution: POLAIR, Int J Environ Pollut, 22, 17,

766 https://doi.org/10.1504/IJEP.2004.005474, 2004.

767 Chang, J. C. and Hanna, S. R.: Air quality model performance evaluation, Meteorology

768 and Atmospheric Physics, 87, 167–196, https://doi.org/10.1007/s00703-003-0070-7,

769 2004.

770 Du, Y., Xu, X., Chu, M., Guo, Y., and Wang, J.: Air particulate matter and

771 cardiovascular disease: The epidemiological, biomedical and clinical evidence,

772 https://doi.org/10.3978/j.issn.2072-1439.2015.11.37, 2016.

773   Ferrero, E., Alessandrini, S., Anderson, B., Tomasi, E., Jimenez, P., and Meech, S.:

774   Lagrangian simulation of smoke plume from fire and validation using ground-based

775   lidar and aircraft measurements, Atmos Environ, 213, 659–674,

776   https://doi.org/10.1016/j.atmosenv.2019.06.049, 2019.

777   Fu, K. and Liang, D.: The conservative characteristic FD methods for atmospheric

778   aerosol transport problems, J Comput Phys, 305, 494–520,

779   https://doi.org/10.1016/j.jcp.2015.10.049, 2016.

780   Gao, S., Kurppa, M., Chan, C. K., and Ngan, K.: Technical note: Dispersion of cooking-

781   generated aerosols from an urban street canyon, Atmos Chem Phys, 22, 2703–2726,

782   https://doi.org/10.5194/acp-22-2703-2022, 2022.

783   Guimet, V. and Laurence, D.: A linearised turbulent production in the k-ε model for

784   engineering applications, in: Engineering Turbulence Modelling and Experiments 5,

785   edited by: Rodi, W. and Fueyo, N., Elsevier Science Ltd, Oxford, UK, 157–166, 2002.

786   Hanna, S. R., Hansen, O. R., and Dharmavaram, S.: FLACS CFD air quality model

787   performance evaluation with Kit Fox, MUST, Prairie Grass, and EMU observations,

788   Atmos Environ, 38, 4675–4687, https://doi.org/10.1016/j.atmosenv.2004.05.041, 2004.

789   Harten, A.: On a Class of High Resolution Total-Variation-Stable Finite-Difference

790   Schemes, SIAM J Numer Anal, 21, 1–23, https://doi.org/10.1137/0721001, 1984.

791   Jones, A. M., Yin, J., and Harrison, R. M.: The weekday–weekend difference and the

792   estimation of the non-vehicle contributions to the urban increment of airborne

793   particulate matter, Atmos Environ, 42, 4467–4479,

794   https://doi.org/10.1016/j.atmosenv.2008.02.001, 2008.

795   Kim, M. J.: Sensitivity of nitrate aerosol production to vehicular emissions in an urban

796   street, Atmosphere (Basel), 10, 212, https://doi.org/10.3390/ATMOS10040212, 2019.

797   Kim, M. J., Park, R. J., Kim, J. J., Park, S. H., Chang, L. S., Lee, D. G., and Choi, J. Y.:

798   Computational fluid dynamics simulation of reactive fine particulate matter in a street

799   canyon, Atmos Environ, 209, 54–66, https://doi.org/10.1016/j.atmosenv.2019.04.013,

800   2019.

801   Kim, Y., Wu, Y., Seigneur, C., and Roustan, Y.: Multi-scale modeling of urban air

802   pollution: development and application of a Street-in-Grid model (v1.0) by coupling

803   MUNICH (v1.0) and Polair3D (v1.8.1), Geosci Model Dev, 11, 611–629,

804   https://doi.org/10.5194/gmd-11-611-2018, 2018.

805   Kim, Y., Lugon, L., Maison, A., Sarica, T., Roustan, Y., Valari, M., Zhang, Y., André,

806   M., Sartelet, K., Paris-saclay, U., and Ecosys, U. M. R.: MUNICH v2.0: A street-

807   network model coupled with SSH-aerosol (v1.2) for multi-pollutant modelling, Geosci

808   Model Dev, 15, 7371-7396, https://doi.org/10.5194/gmd-15-7371-2022, 2022.

809   Kumar, P., Fennell, P., Langley, D., and Britter, R.: Pseudo-simultaneous measurements

810   for the vertical variation of coarse, fine and ultrafine particles in an urban street canyon,

811   Atmos Environ, 42, 4304–4319, https://doi.org/10.1016/j.atmosenv.2008.01.010, 2008.

812   Kurppa, M., Hellsten, A., Roldin, P., Kokkola, H., Tonttila, J., Auvinen, M., Kent, C.,

813   Kumar, P., Maronga, B., and Järvi, L.: Implementation of the sectional aerosol module

814   SALSA2.0 into the PALM model system 6.0: Model development and first evaluation,

815   Geosci Model Dev, 12, 1403–1422, https://doi.org/10.5194/gmd-12-1403-2019, 2019.

816   Lo, K. W. and Ngan, K.: Characterising the pollutant ventilation characteristics of street

817   canyons using the tracer age and age spectrum, Atmos Environ, 122, 611–621,

818   https://doi.org/10.1016/j.atmosenv.2015.10.023, 2015.

819   Lo, K. W. and Ngan, K.: Characterizing ventilation and exposure in street canyons using

820   Lagrangian particles, J Appl Meteorol Climatol, 56, 1177–1194,

821   https://doi.org/10.1175/JAMC-D-16-0168.1, 2017.

822   Lugon, L., Vigneron, J., Debert, C., Chrétien, O., and Sartelet, K.: Black carbon

823   modeling in urban areas: investigating the influence of resuspension and non-exhaust

824   emissions in streets using the Street-in-Grid model for inert particles (SinG-inert),

825   Geosci Model Dev, 14, 7001–7019, https://doi.org/10.5194/gmd-14-7001-2021, 2021a.

826   Lugon, L., Sartelet, K., Kim, Y., Vigneron, J., and Chretien, O.: Simulation of primary

827   and secondary particles in the streets of Paris using MUNICH, Faraday Discuss, 226,

828   432–456, https://doi.org/10.1039/d0fd00092b, 2021b.

829   Maison, A., Flageul, C., Carissimo, B., Wang, Y., Tuzet, A., and Sartelet, K.:

830   Parameterizing the aerodynamic effect of trees in street canyons for the street network

831   model MUNICH using the CFD model Code_Saturne, Atmos Chem Phys, 22, 9369–

832   9388, https://doi.org/10.5194/acp-22-9369-2022, 2022.

833   OpenFOAM user guide: https://www.openfoam.com/.

834   Parente, A., Gorlé, C., van Beeck, J., and Benocci, C.: Improved k–ε model and wall

835   function formulation for the RANS simulation of ABL flows, Journal of Wind

836   Engineering and Industrial Aerodynamics, 99, 267–278,

837   https://doi.org/10.1016/j.jweia.2010.12.017, 2011.

838   Di Sabatino, S., Buccolieri, R., Pulvirenti, B., and Britter, R.: Simulations of pollutant

839   dispersion within idealised urban-type geometries with CFD and integral models, Atmos

840   Environ, 41, 8316–8329, https://doi.org/10.1016/j.atmosenv.2007.06.052, 2007.

841   Sartelet, K., Zhu, S., Moukhtar, S., André, M., André, J. M., Gros, V., Favez, O.,

842   Brasseur, A., and Redaelli, M.: Emission of intermediate, semi and low volatile organic

843   compounds from traffic and their impact on secondary organic aerosol concentrations

844   over Greater Paris, Atmos Environ, 180, 126–137,

https://doi.org/10.1016/j.atmosenv.2018.02.031, 2018.

Sartelet, K., Couvidat, F., Wang, Z., Flageul, C., and Kim, Y.: SSH-aerosol v1.1: A modular box model to simulate the evolution of primary and secondary aerosols, Atmosphere (Basel), 11, 525, https://doi.org/10.3390/atmos11050525, 2020.

Sartelet, K. N., Debry, E., Fahey, K., Roustan, Y., Tombette, M., and Sportisse, B.: Simulation of aerosols and gas-phase species over Europe with the Polyphemus system: Part I-Model-to-data comparison for 2001, Atmos Environ, 41, 6116–6131, https://doi.org/10.1016/j.atmosenv.2007.04.024, 2007.

Sportisse, B.: An Analysis of Operator Splitting Techniques in the Stiff Case, J Comput Phys, 161, 140–168, https://doi.org/10.1006/jcph.2000.6495, 2000.

Stelson, A. W. and Seinfeld, J. H.: Relative humidity and temperature dependence of the ammonium nitrate dissociation constant, Atmospheric Environment (1967), 16, 983–992, https://doi.org/10.1016/0004-6981(82)90184-6, 1982.

Suarez-Bertoa, R. and Astorga, C.: Impact of cold temperature on Euro 6 passenger car emissions, Environmental Pollution, 234, 318–329, https://doi.org/10.1016/j.envpol.2017.10.096, 2018.

Suarez-Bertoa, R., Mendoza-Villafuerte, P., Riccobono, F., Vojtisek, M., Pechout, M., Perujo, A., and Astorga, C.: On-road measurement of NH 3 emissions from gasoline and diesel passenger cars during real world driving conditions, Atmos Environ, 166, 488–497, https://doi.org/10.1016/j.atmosenv.2017.07.056, 2017.

Sun, K., Tao, L., Miller, D. J., Pan, D., Golston, L. M., Zondlo, M. A., Griffin, R. J., Wallace, H. W., Leong, Y. J., Yang, M. M., Zhang, Y., Mauzerall, D. L., and Zhu, T.: Vehicle Emissions as an Important Urban Ammonia Source in the United States and China, Environ Sci Technol, 51, 2472–2481, https://doi.org/10.1021/acs.est.6b02805, 2017.

Sung, J. C., Pulliam, B. L., and Edwards, D. A.: Nanoparticles for drug delivery to the lungs, Trends Biotechnol, 25, 563–570, https://doi.org/10.1016/j.tibtech.2007.09.005, 2007.

Tominaga, Y. and Stathopoulos, T.: Turbulent Schmidt numbers for CFD analysis with various types of flowfield, Atmos Environ, 41, 8091–8099, https://doi.org/10.1016/j.atmosenv.2007.06.054, 2007.

Tominaga, Y. and Stathopoulos, T.: CFD simulation of near-field pollutant dispersion in the urban environment: A review of current modeling techniques, Atmos Environ, 79, 716–730, https://doi.org/10.1016/j.atmosenv.2013.07.028, 2013.

Trini Castelli, S., Armand, P., Tinarelli, G., Duchenne, C., and Nibart, M.: Validation of a Lagrangian particle dispersion model with wind tunnel and field experiments in urban

881 environment, Atmos Environ, 193, 273–289,

882 https://doi.org/10.1016/j.atmosenv.2018.08.045, 2018.

883 Wesely, M. L.: Parameterization of surface resistances to gaseous dry deposition in

884 regional-scale numerical models, Atmospheric Environment (1967), 23, 1293–1304,

885 https://doi.org/10.1016/0004-6981(89)90153-4, 1989.

886 Wu, L., Hang, J., Wang, X., Shao, M., and Gong, C.: APFoam 1.0: Integrated

887 computational fluid dynamics simulation of O3-NOx-volatile organic compound

888 chemistry and pollutant dispersion in a typical street canyon, Geosci Model Dev, 14,

889 4655–4681, https://doi.org/10.5194/gmd-14-4655-2021, 2021.

890 Yakhot, V., Orszag, S. A., Thangam, S., Gatski, T. B., and Speziale, C. G.: Development

891 of turbulence models for shear flows by a double expansion technique, Physics of Fluids

892 A, 4, 1510–1520, https://doi.org/10.1063/1.858424, 1992.

893 Yee, H. C.: Construction of explicit and implicit symmetric TVD schemes and their

894 applications, J Comput Phys, 68, 151–179, https://doi.org/10.1016/0021-

895 9991(87)90049-0, 1987.

896 Zhang, K., Chen, G., Zhang, Y., Liu, S., Wang, X., Wang, B., and Hang, J.: Integrated

897 impacts of turbulent mixing and NOX-O3 photochemistry on reactive pollutant

898 dispersion and intake fraction in shallow and deep street canyons, Science of The Total

899 Environment, 712, 135553, https://doi.org/10.1016/j.scitotenv.2019.135553, 2020.

900 Zhang, L., Gong, S., Padro, J., and Barrie, L.: A size-segregated particle dry deposition

901 scheme for an atmospheric aerosol module, Atmos Environ, 35, 549–560,

902 https://doi.org/10.1016/S1352-2310(00)00326-5, 2001.

903 Zhang, L., Brook, J. R., and Vet, R.: A revised parameterization for gaseous dry

904 deposition in air-quality models, Atmos Chem Phys, 3, 2067–2082,

905 https://doi.org/10.5194/acp-3-2067-2003, 2003.

906

907 Appendix A

908 The schemes for particle deposition velocity v_d were added to the transport equations

909 using volume sink terms based on (Zhang et al., 2001) and can be represented as:

$$v_{d,p} = \begin{cases} v_g + \dfrac{1}{R_a + R_s}, & \text{Wall surfaces} \\ v_g, & \text{Entire field} \end{cases} \tag{A1}$$

$$v_g = \frac{\rho d_p^2 g C}{18\eta} \tag{A2}$$

$$R_a = \frac{\ln(z_R/z_0) - \psi_H}{\kappa u_*} \tag{A3}$$

$$R_s = \frac{1}{\varepsilon_0 u_* (E_B + E_{IM} + E_{IN}) R_1} \tag{A4}$$

910   The deposition velocity for the particles $v_{d,p}$ consists of both gravitational settling and
911   surface deposition near the wall surfaces. The gravitational settling velocity v_g was
912   considered for the entire field, ρ is the particle density; d_p is the particle diameter; g
913   is the acceleration of gravity; C is Cunningham correction factor for small particles; η
914   is the viscosity coefficient of air.
915   The aerodynamic resistance R_a is calculated from the first-layer-height z_R, roughness
916   length z_0, Von Kármán constant κ, friction velocity u_* and stability function ψ_H. For the
917   k–ε model, u_* is estimated by $\left(C_\mu^{0.5} k\right)^{0.5}$ and $C_\mu = 0.09$ is a constant of the model.
918   The surface resistance R_s is calculated from u_*, the collection efficiency from Brownian
919   diffusion E_B, the impaction E_{IM} and the interception E_{IN}. The correction factor
920   represents the fraction of particles that stick to the surface R_1 and an empirical
921   constant $\varepsilon_0 = 3$.
922   The dry deposition schemes for gas were added to the transport equations using volume
923   sink terms based on (Wesely, 1989) and (Zhang et al., 2003),which can be represented as:

$$v_{d,g} = \frac{1}{R_a + R_b + R_c} \tag{A5}$$

$$R_b = \frac{2}{\kappa u_*} \left(\frac{Sc}{Pr}\right)^{2/3} \tag{A6}$$

924   The deposition velocity for gas $v_{d,g}$ is calculated from the aerodynamic resistance R_a,
925   the quasi-laminar layer resistance R_b and the surface resistance for gas R_c. $Sc = v/D$
926   and $Pr = 0.72$ are the Schmidt and Prandtl number. v is the kinematic viscosity of air
927   and D is the molecular diffusivity of different gases. R_c is calculated based on (Zhang
928   et al., 2003).
929

930   Appendix B
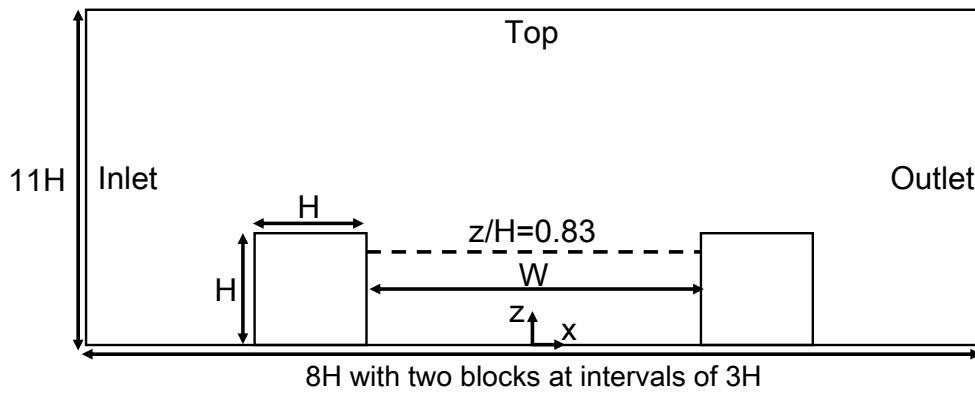
931
932   Fig. B1 Simulation domain for velocity validation.
933
934   Correctly representing the flow field in the street canyon is important to model accurately
935   the concentrations. Unfortunately, observation data on wind velocity is the street is not
936   available. Therefore, we conducted a velocity validation for OpenFOAM v2012 using
937   data from a wind tunnel experiment (Blackman et al., 2015). The 2-D simulation domain
938   is shown in Fig. B1. The aspect ratio in the experiment (H/W=0.33) is close to this study
939   (H/W=0.31). The building height H is 0.06 m. The grid size is 1/20 H in x- and z-
940   directions in the simulation domain under $3H$. The free-stream velocity U_{ref} is 5.9 m/s.
941   The steady-state flow field is simulated with the same turbulence model (RNG k–ε model)
942   as in the paper, and cyclic boundary conditions are used for the inlet and outlet. The slip
943   boundary is considered for the top, and non-slip boundary conditions with the same wall
944   functions as in the paper are considered for other walls.
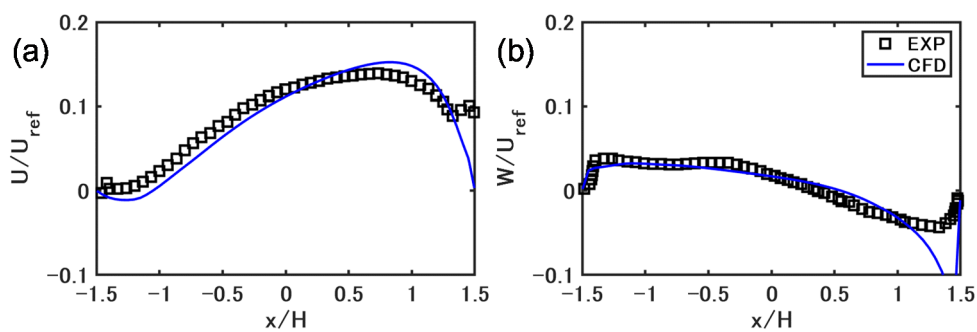
945
946   Fig. B2 Streamwise and vertical direction of mean wind velocities at $z/H = 0.83$.
947
948   Fig. B2 compares the simulated streamwise and vertical direction of mean wind velocities
949   with the experimental values at $z/H = 0.83$. The RNG k–ε model reproduce well the
950   velocities, although the velocities very close to the windward wall show differences with

951   the experimental values. The above validation shows that if suitable inlet conditions are

952   given, the flow field is well reproduced with the turbulence model adopted in this study.